

A Finite Volume Error Estimator Inspired by the Variational Multiscale Approach

Oriol Colomés*, Guglielmo Scovazzi†, Ihab Sraj‡ and Omar Knio§

Duke University, Durham (NC), USA.

Olivier Le Maître¶

LIMSI-CNRS, Université Paris Saclay, Orsay, France.

In this work, we define a family of explicit *a posteriori* error estimators for Finite Volume methods in computational fluid dynamics. The proposed error estimators are inspired by the Variational Multiscale method, originally defined in a Finite Element context. The proposed error estimators are tested in simulations of the incompressible Navier-Stokes equations, the thermally-coupled Navier-Stokes equations, and the fully-coupled compressible large eddy simulation of the HIFiRE Direct Connect Rig Scramjet combustor.

I. Introduction

Computational fluid dynamics (CFD) is widely applied in the aerospace/automotive/chemical engineering, power generation, medical research, meteorology or astrophysics. In particular, incompressible or compressible fluid flows are often coupled with thermal engineering, combustion, radiation or multi-phase problems, among others.

CFD relies on the definition of a mathematical model that describes the fluid motion, from which a solution is obtained using approximation techniques such as Finite Difference (FD), Finite Volume (FV), or Finite Element (FE) methods.

The approximated solution, also called numerical solution hereinafter, differs in general from the true solution. Let ϕ_{true} be a quantity (or field) of interest that represents a certain physical phenomenon, e.g. the velocity field of a fluid. Let ϕ_{mod} be the quantity of interest given by the mathematical model that describes the physical phenomenon. The numerical solution is computed on a certain mesh, that is a subdivision of the computational domain into smaller portions of characteristic size, h . We will denote as ϕ_h the numerical solution of the quantity of interest ϕ_{mod} . Following Celik *et al.*,¹ we can distinguish between two types of error that are responsible of the difference between the true solution and the numerical solution (ε): the numerical error, ε_{num} , and the model error, ε_{mod} .

$$\varepsilon = \phi_{\text{true}} - \phi_h = \varepsilon_{\text{mod}} + \varepsilon_{\text{num}}, \quad (1a)$$

$$\varepsilon_{\text{num}} = \phi_{\text{mod}} - \phi_h, \quad (1b)$$

$$\varepsilon_{\text{mod}} = \phi_{\text{true}} - \phi_{\text{mod}}. \quad (1c)$$

The numerical error includes the discretization error (both in space and time), denoted as $\varepsilon_{\text{disc}}$, the iterative convergence error, $\varepsilon_{\text{conv}}$, and round-off error, $\varepsilon_{\text{roun}}$. In order to determine the error of the numerical approximation, each source of error should be taken into account, i.e. $\varepsilon_{\text{num}} = \varepsilon_{\text{disc}} + \varepsilon_{\text{conv}} + \varepsilon_{\text{roun}}$. In practical

*Postdoctoral Associate, Department of Civil and Environmental Engineering.

†Associate Professor, Department of Civil and Environmental Engineering, and Department of Mechanical Engineering and Materials Science.

‡Research Scientist, Department of Mechanical Engineering and Materials Science

§Adjunct Professor, Department of Civil and Environmental Engineering, and Department of Mechanical Engineering and Materials Science.

¶Senior researcher, Mechanics and Energetic Department.

situations, the convergence and round-off errors are small and easy to determine, therefore, the numerical error will be dominated by the discretization error. In what follows, we will not distinguish between numerical and discretization error, assuming that $\varepsilon_{\text{num}} \approx \varepsilon_{\text{disc}}$.

From (1a) we see that the true solution is approximated by the numerical solution up to an error, $\phi_{\text{true}} = \phi_h + \varepsilon$. Since, in general, we cannot obtain an exact value of the error, we say that the numerical solution reproduces the true solution with an uncertainty. The characterization of this uncertainty is crucial to take decisions in most of the engineering problems, and it is precisely the goal of the uncertainty quantification (UQ) field.

According to Celik *et al.*,¹ we can distinguish between two different approaches that aim to quantify the numerical uncertainty. The first approach relies on probabilistic methods, see for instance the work done by Rebba *et al.*² The second approach relies in deterministic methods based on error estimators, see *e.g.* Roache³ and Oden *et al.*⁴ In this work, we will describe a family of deterministic error estimators to characterize the discretization error.

Since the first developments on the definition of *a posteriori* error estimators for FE methods done by Babuska and Rheinboldt,⁵ many works have been published over the last few decades. In the work done by Ainsworth and Oden,⁶ a wide overview of *a posteriori* error estimator for FE is given. Other reviews on *a posteriori* error estimators can be found, for instance, in Roy⁷ or Verfurth.⁸ Hauke and co-workers⁹ introduced the variational multiscale (VMS) method¹⁰ for the *a posteriori* error estimation of numerical simulations. This approach was then extended to multi-dimensional transport problems,¹¹ and to the Euler and Navier-Stokes (NS) equations.¹² Recently, a pointwise error estimator based on the VMS error estimators has also been proposed by Irisarri *et al.*¹³ The VMS method was firstly introduced as a stabilization method in the FE community by Hughes.¹⁰ Since then, many contributions have been used this approach in different contexts, and in particular, to the simulation of turbulent flows, which is the flow type targeted in the current work. Some examples can be found in Bazilevs *et al.*,¹⁴ Colomés *et al.*¹⁵ or Rasthofer *et al.*¹⁶ In the cited works, the VMS method is also presented as an Implicit Large Eddy Simulation (ILES) method, which could open the door to the understanding of the VMS error estimator, not only as a numerical error, but also as a model error. However, this aspect will not be discussed in this paper.

In this work we will assess the behaviour of VMS error estimators for the fluid flow simulations, but rather than using the traditional FE discretization, we extend the use of VMS error estimators to the case of FV methods, starting from the incompressible NS equations, and extending it to the investigation of thermally-coupled flows and compressible NS equations.

Therefore, the main goal of this work is the definition of *a posteriori* and non-intrusive error estimators, based on the VMS methodology, for their application to fluid flow simulations in a FV context. The paper is structured as follows: first we describe the VMS framework for the incompressible NS equations in Section II. The definition of the VMS error estimators in a FE context is recalled in Section III, and followed by its extension in a FV context, as presented in Section IV. Some numerical results are shown for the incompressible, thermally-coupled and compressible NS equations in Section V. Finally, the overall conclusions and further work are stated in Section VI.

II. The variational multiscale method

In this section we state the VMS framework for the incompressible NS equations, which will be later used for the derivation of the VMS error estimators. The extension to thermally-coupled flows can be found in Codina *et al.*,¹⁷ and, for the compressible NS equations, in Koobus *et al.*¹⁸

Let us consider the spatial domain Ω with boundaries $\Gamma_D \oplus \Gamma_N = \Gamma$, where Γ_D is the Dirichlet (essential) boundary and Γ_N the Neumann (natural) boundary. The strong form of the unsteady incompressible NS equations reads, find the velocity field, \mathbf{u} , and the pressure field, p , such that

$$\begin{aligned} \partial_t \mathbf{u} - \nu \Delta \mathbf{u} + \mathbf{u} \cdot \nabla \mathbf{u} + \nabla p &= \mathbf{f} && \text{in } \Omega, \\ \nabla \cdot \mathbf{u} &= 0 && \text{in } \Omega, \\ \mathbf{u} &= \mathbf{u}_g && \text{on } \Gamma_D, \\ \mathcal{B}(\mathbf{u}, p) &= \mathbf{h} && \text{on } \Gamma_N, \end{aligned} \tag{2}$$

where ν is the viscosity, \mathbf{u}_g a given function defined on the Dirichlet boundary Γ_D , \mathbf{h} a given function defined on the boundary Γ_N and \mathbf{f} the external source term defined in Ω . Furthermore, $\mathcal{B}(\mathbf{u}, p) := (p\mathbf{I} + \nabla^s \mathbf{u}) \cdot \mathbf{n}$

is the Neumann boundary operator acting over \mathbf{u} and p , which will be defined later. Let us define the NS operator as

$$\mathcal{L}(\mathbf{u}, p) := \begin{bmatrix} \mathcal{L}_m(\mathbf{u}, p) \\ \mathcal{L}_c(\mathbf{u}) \end{bmatrix},$$

where $\mathcal{L}_m(\mathbf{u}, p) := \partial_t \mathbf{u} - \nu \Delta \mathbf{u} + \mathbf{u} \cdot \nabla \mathbf{u} + \nabla p$ is the momentum operator and $\mathcal{L}_c(\mathbf{u}) := \nabla \cdot \mathbf{u}$ the incompressibility constraint operator. The weak form of the problem (2) can be stated as:

Find $\mathbf{u} \in \mathcal{V}_g$ and $p \in \mathcal{Q}$ such that

$$B([\mathbf{v}, q], [\mathbf{u}, p]) = (\mathbf{v}, \mathbf{f}) + (\mathbf{v}, \mathbf{h})_{\Gamma_N}, \quad \forall \mathbf{v} \in \mathcal{V}_0, \quad \forall q \in \mathcal{Q}, \quad (3)$$

where $B(\cdot, \cdot)$ is the bilinear form defined as

$$B([\mathbf{v}, q], [\mathbf{u}, p]) := (\mathbf{v}, \mathcal{L}_m(\mathbf{u}, p)) + (q, \mathcal{L}_c(\mathbf{u})) + (\mathbf{v}, \mathcal{B}(\mathbf{u}, p))_{\Gamma_N}, \quad (4)$$

and the set of variational spaces \mathcal{V}_g , \mathcal{V}_0 and \mathcal{Q} are defined as

$$\mathcal{V}_g := \{\mathbf{v} \in \mathbf{H}^1(\Omega) : \mathbf{v}|_{\Gamma_D} = \mathbf{u}_g\} \equiv \mathbf{H}_g^1(\Omega), \quad (5)$$

$$\mathcal{V}_0 := \{\mathbf{v} \in \mathbf{H}^1(\Omega) : \mathbf{v}|_{\Gamma_D} = 0\} \equiv \mathbf{H}_0^1(\Omega), \quad (6)$$

$$\mathcal{Q} := L^2(\Omega)/\mathbb{R}. \quad (7)$$

In (5)-(6) bold characters are used to denote vectorial spaces, *i.e.* $\mathbf{H}^m(\Omega) := \{\mathbf{H}^m(\Omega)\}^d$, where d is the number of spatial dimensions.

We consider a finite element partition \mathcal{T}_h of the domain Ω from which we can construct a conforming Finite Element (FE) space $\mathcal{V}_h \subset \mathcal{V}$. Let $\mathcal{E}_h = \cup_{K \in \mathcal{T}_h} \partial K$ be the set of the faces (or edges in 2D) of the mesh and $\mathcal{E}_h^0 = \mathcal{E}_h \setminus \Gamma$.

The VMS method¹⁰ relies on the decomposition of the variational spaces (5)-(7) into the resolved (FE solution) and unresolved (error) scales, $\mathcal{V}_0 = \mathcal{V}_{0,h} + \mathcal{V}'_0$ and $\mathcal{Q} = \mathcal{Q}_h + \mathcal{Q}'$, respectively. Applying this decomposition to the solution fields \mathbf{u} and p , and the test functions \mathbf{v} and q , and introducing the result into (3) we obtain the following problems:

$$B([\mathbf{v}_h, q_h], [\mathbf{u}_h, p_h]) = -B([\mathbf{v}_h, q_h], [\mathbf{u}', p']) + (\mathbf{v}_h, \mathbf{f}) + (\mathbf{v}_h, \mathbf{h})_{\Gamma_N} \quad \forall \mathbf{v}_h \in \mathcal{V}_{0,h}, \quad \forall q_h \in \mathcal{Q}_h, \quad (8)$$

$$B([\mathbf{v}', q'], [\mathbf{u}', p']) = -B([\mathbf{v}', q'], [\mathbf{u}_h, p_h]) + (\mathbf{v}', \mathbf{f}) + (\mathbf{v}', \mathbf{h})_{\Gamma_N} \quad \forall \mathbf{v}' \in \mathcal{V}'_0, \quad \forall q' \in \mathcal{Q}'. \quad (9)$$

Now, problem (9) is defined on an infinite-dimensional space and its solution is not readily computable. Thus, in order to obtain a solution, we model the subscale component by means of an approximate Green's function approach. As initially proposed by Hughes,¹⁰ from equation (9), the Green's function can be approximated by a model for the flow subgrid time-scales:

$$\mathbf{u}' \approx \tau_m \mathcal{P}(\mathbf{f} - \mathcal{L}_m(\mathbf{u}_h, p_h)), \quad (10)$$

$$p' \approx \tau_c \mathcal{P}(-\mathcal{L}_c(\mathbf{u}_h)). \quad (11)$$

Here \mathcal{P} is a certain projection into the subscales space, and τ_m and τ_c are approximations to the mean elemental value of the Green's functions, namely,

$$\tau_m^K \approx \frac{1}{\text{meas}(\Omega^K)} \int_{\Omega^K} \mathbf{g}'_u(\mathbf{x}, \mathbf{y}) d\Omega, \quad (12)$$

$$\tau_c^K \approx \frac{1}{\text{meas}(\Omega^K)} \int_{\Omega^K} \mathbf{g}'_p(\mathbf{x}, \mathbf{y}) d\Omega. \quad (13)$$

Various definitions of τ_m and τ_c have been proposed.^{19,20} In this work we will consider the definition of the stabilization parameter given by Codina,²¹ which is defined as $\tau_m = \tau_m \mathcal{I}$, with \mathcal{I} the identity operator,

$$\tau_m = \left(\frac{c_1 \nu}{h^2} + \frac{c_2 |\mathbf{u}|}{h} \right)^{-1} \quad \text{and} \quad \tau_c = \frac{h^2}{c_1 \tau_m}.$$

Here c_1 and c_2 are two algorithmic constants, usually taken as $c_1 = 4$ and $c_2 = 2$.

Remark. In this work we will only consider the case in which the projection appearing in (10)-(11) is the identity operator, $\mathcal{P} \equiv \mathcal{I}$. This choice is the standard definition used in Hughes,¹⁰ and often called algebraic subgrid scales (ASGS) method, see Codina.²² However, alternative projection definitions can be used. In the work done by Codina,²⁰ a particular definition of the space of the subscales is considered in a such a way that $\mathcal{V}' \approx \mathcal{V}_h^\perp$, *i.e.* the space of the subscales is considered to be orthogonal to the FE space (OSS) method. With this choice, less numerical diffusion is introduced compared with the ASGS method while being equally stable, see Colomés *et al.*¹⁵

Plugging back equations (10)-(11) into (8) we obtain a closed expression for $[\mathbf{u}_h, p_h]$ for which we can compute the solution

$$\begin{aligned} & B([\mathbf{v}_h, q_h], [\mathbf{u}_h, p_h]) - (\mathcal{L}_m^*(\mathbf{v}_h, q_h), \boldsymbol{\tau}_m \mathcal{L}_m(\mathbf{u}_h, p_h))_{\tilde{\Omega}} - (\mathcal{L}_c^*(\mathbf{v}_h), \boldsymbol{\tau}_c \mathcal{L}_c(\mathbf{u}_h))_{\tilde{\Omega}} \\ & = (\mathbf{v}_h, \mathbf{f})_{\Omega} - (\mathcal{L}_m^*(\mathbf{v}_h, q_h), \boldsymbol{\tau}_m \mathbf{f})_{\tilde{\Omega}} + (\mathbf{v}_h, \mathbf{h})_{\Gamma_N} \quad \forall \mathbf{v}_h \in \mathcal{V}_{0,h}, \quad \forall q_h \in \mathcal{Q}_h, \end{aligned} \quad (14)$$

with $\mathcal{L}_m^*(\mathbf{v}, q) := -\nu \Delta \mathbf{v} - \mathbf{u} \cdot \nabla \mathbf{v} - \nabla q$ the adjoint momentum operator and $\mathcal{L}_c^*(\mathbf{v}) := -\nabla \cdot \mathbf{v}$ the adjoint operator of the incompressibility constraint. Note that $\tilde{\Omega} := \bigcup_K^{N_{el}} \Omega^K$ is the union of all the mesh elements and $\tilde{\Gamma} := \bigcup_K^{N_{el}} \Gamma^K \setminus \Gamma$ the union of inter-element boundaries that do not lay on the domain boundary.

Remark. In (14), we neglected the effect of the inter-element boundary terms on the subscales, that is, we assumed $\mathbf{v}' = 0$ on Γ^K in equation (9). As shown by Codina *et al.*,²³ these terms do not affect the accuracy of the solution, and they are only crucial to guarantee stability when discontinuous pressure interpolations are used.

III. Variational multiscale error estimators

The VMS framework also allows us to define estimates of the error, since the subscale can be thought of as the error associated with the coarse scale approximation of the velocity and pressure fields, $\mathbf{e}_u = \mathbf{u}' = \mathbf{u} - \mathbf{u}_h$ and $e_p = p' = p - p_h$, respectively. Next, we recall the definition of error estimators based on the VMS method in the work done by Hauke *et al.*¹²

From (9), using the Green's function as proposed in Hughes,¹⁰ we can obtain an analytical expression for the subscales \mathbf{u}' and p' as

$$\begin{aligned} \mathbf{u}'(\mathbf{x}) &= - \int_{\tilde{\Omega}} \mathbf{g}'_u(\mathbf{x}, \mathbf{y})(\mathcal{L}_m(\mathbf{u}_h) - \mathbf{f})(\mathbf{y})d\Omega - \int_{\tilde{\Gamma}} \mathbf{g}'_u(\mathbf{x}, \mathbf{y})([\mathcal{B}(\mathbf{u}_h, p_h)])(\mathbf{y})d\Gamma \\ &\quad - \int_{\Gamma_N} \mathbf{g}'(\mathbf{x}, \mathbf{y})(\mathcal{B}(\mathbf{u}_h, p_h) - \mathbf{h})(\mathbf{y})d\Gamma, \end{aligned} \quad (15)$$

$$p'(\mathbf{x}) = - \int_{\tilde{\Omega}} \mathbf{g}'_p(\mathbf{x}, \mathbf{y})(\mathcal{L}_c(\mathbf{u}_h))(\mathbf{y})d\Omega. \quad (16)$$

In equations (15)-(16), we can distinguish the contribution from the element interior integrals and the element boundaries integrals and decompose the subscales as the sum of the element interior and the inter-element boundary contributions

$$\mathbf{u}' = \mathbf{u}'_K + \mathbf{u}'_{\partial K}, \quad (17)$$

$$p' = p'_K + p'_{\partial K}, \quad (18)$$

with

$$\mathbf{u}'_K(\mathbf{x}) = - \int_{\tilde{\Omega}} \mathbf{g}'_u(\mathbf{x}, \mathbf{y})(\mathcal{L}_m(\mathbf{u}_h) - \mathbf{f})(\mathbf{y})d\Omega, \quad (19)$$

$$\mathbf{u}'_{\partial K}(\mathbf{x}) = - \int_{\tilde{\Gamma}} \mathbf{g}'_u(\mathbf{x}, \mathbf{y})([\mathcal{B}(\mathbf{u}_h, p_h)])(\mathbf{y})d\Gamma - \int_{\Gamma} \mathbf{g}'(\mathbf{x}, \mathbf{y})(\mathcal{B}(\mathbf{u}_h, p_h) - \mathbf{h})(\mathbf{y})d\Gamma, \quad (20)$$

$$p'_K(\mathbf{x}) = - \int_{\tilde{\Omega}} \mathbf{g}'_p(\mathbf{x}, \mathbf{y})(\mathcal{L}_c(\mathbf{u}_h))(\mathbf{y})d\Omega, \quad (21)$$

$$p'_{\partial K}(\mathbf{x}) = 0. \quad (22)$$

For a certain norm, $\|\cdot\|_{\mathbf{L}^r(\Omega)}$, with $r \in \mathbb{N}$, we can find an upper bound for the subscales norm making use of the triangle inequality in the subscale decomposition (17)-(18):

$$\|\mathbf{u}'\|_{\mathbf{L}^r(\Omega)} \leq \|\mathbf{u}'_K\|_{\mathbf{L}^r(\Omega)} + \|\mathbf{u}'_{\partial K}\|_{\mathbf{L}^r(\Omega)}, \quad (23)$$

$$\|p'\|_{\mathbf{L}^r(\Omega)} \leq \|p'_K\|_{\mathbf{L}^r(\Omega)} + \|p'_{\partial K}\|_{\mathbf{L}^r(\Omega)}. \quad (24)$$

Therefore, a bound of the error (subscales) can be derived by bounding both the interior and the inter-element boundary subscale contributions. Starting from the exact equations (19) and (21), taking the absolute value of each component, applying the Hölders inequality and applying the Green's function norm, we arrive to the following estimate (see Hauke *et al.*¹² for details)

$$\|\mathbf{u}'_K\|_{\mathbf{L}^r(K)} \leq \text{meas}(K)^{1/r} \tau_{m,L^r}^+ \|(\mathcal{L}_m(\mathbf{u}_h) - \mathbf{f})\|_{\mathbf{L}^\infty(K)}, \quad (25)$$

$$\|p'_K\|_{\mathbf{L}^r(K)} \leq \text{meas}(K)^{1/r} \tau_{c,L^r}^+ \|(\mathcal{L}_c(\mathbf{u}_h))\|_{\mathbf{L}^\infty(K)}, \quad (26)$$

with $\tau_{ij}^+ = \max_K(0, \tau_{ij})$. In this work we will focus on the \mathbf{L}^2 -norm of the error, from which the time-scale parameters take the following expression: $\tau_{m,L^2} = \min\left(\frac{h}{\sqrt{3}|\mathbf{u}_h|}, \frac{h^2}{24.24\nu}\right)$, and $\tau_{c,L^2} = \frac{h_c^2}{4\tau_m}$, with h_c as defined in Hauke *et al.*¹² The inter-element boundaries error will be bounded by the following expression

$$\|\mathbf{u}'_{\partial K}\|_{\mathbf{L}^r(K)} \leq \text{meas}(K)^{1/r} \tau_{m,L^r}^+ \frac{1}{2} \frac{\text{meas}(\partial K)}{\text{meas}(K)} \|[\mathcal{B}(\mathbf{u}_h, p_h)]\|_{\mathbf{L}^\infty(\partial K)}. \quad (27)$$

Here we consider only the \mathbf{L}^2 -norm ($r = 2$), but other choices are possible, see Hauke.²⁴ In this case, the final expression for the VMS error estimator reads

$$\eta_{K,\mathbf{u}} = \text{meas}(K)^{1/2} \tau_{m,L^2}^+ \left(\|\mathbf{f} - \mathcal{L}_m(\mathbf{u}_h, p_h)\|_{L^\infty(K)} + \frac{1}{2} \frac{\text{meas}(\partial K)}{\text{meas}(K)} \|[\mathcal{B}(\mathbf{u}_h, p_h)]\|_{L^\infty(K)} \right), \quad (28)$$

$$\eta_{K,p} = \text{meas}(K)^{1/2} \tau_{c,L^2}^+ \left(\|\mathcal{L}_c(\mathbf{u}_h)\|_{L^\infty(K)} \right). \quad (29)$$

Remark. The inter-element boundaries errors do not play a relevant role for convection dominated problems.

IV. VMS error estimators in a Finite Volume framework

In this section we consider the extension of the VMS error estimators for the Navier-Stokes equations into a FV framework. In order to keep the problem simple, here we will consider only the interior element contribution of the simplified VMS version of the error estimator, *i.e.*,

$$\eta_{K,\mathbf{u}} = \text{meas}(K)^{1/2} \tau_{m,L^2}^+ \left(\|\mathbf{f} - \mathcal{L}_m(\mathbf{u}_h, p_h)\|_{L^\infty(K)} \right), \quad (30)$$

$$\eta_{K,p} = \text{meas}(K)^{1/2} \tau_{c,L^2}^+ \left(\|\mathcal{L}_c(\mathbf{u}_h)\|_{L^\infty(K)} \right). \quad (31)$$

Note that this simplification is valid when high Reynolds numbers are used, which is the case of main interest for us. The expression of $\eta_{K,\mathbf{u}}$ and $\eta_{K,p}$ for the NS equations depend on the \mathbf{L}^∞ -norm of the momentum and continuity residuals, respectively, which are given by

$$\mathcal{R}_m(\mathbf{u}_h, p_h) = \mathbf{f} - \mathcal{L}_m(\mathbf{u}_h, p_h) = \mathbf{f} - [\partial_t \mathbf{u}_h - \nu \Delta \mathbf{u}_h + \mathbf{u}_h \cdot \nabla \mathbf{u}_h + \nabla p_h], \quad (32)$$

$$\mathcal{R}_c(\mathbf{u}_h) = -\mathcal{L}_c(\mathbf{u}_h) = -\nabla \cdot \mathbf{u}_h. \quad (33)$$

In a FV context, we assume that the residual is piecewise constant, *i.e.* constant over each cell. Under this assumption we have that for any cell K , the \mathbf{L}^∞ -norm is equivalent to the \mathbf{L}^1 -norm, *i.e.* $\|\cdot\|_{\mathbf{L}^\infty(K)} \equiv \|\cdot\|_{\mathbf{L}^1(K)}$. Moreover, also assuming piecewise constant residuals, we have that $\mathcal{R}_m(\mathbf{u}_h, p_h)|_K \equiv \frac{1}{\text{meas}(K)} \int_K \mathcal{R}_m(\mathbf{u}_h, p_h) d\Omega$. Thus, on a given cell K of the FV discretization, the \mathbf{L}^∞ -norm of the residuals can be expressed as

$$\|\mathcal{R}_m(\mathbf{u}_h, p_h)\|_{\mathbf{L}^\infty(K)} = |\mathcal{R}_m(\mathbf{u}_h, p_h)|_K = \left| \frac{1}{\text{meas}(K)} \int_K \mathcal{R}_m(\mathbf{u}_h, p_h) d\Omega \right|, \quad (34)$$

$$\|\mathcal{R}_c(\mathbf{u}_h)\|_{\mathbf{L}^\infty(K)} = |\mathcal{R}_c(\mathbf{u}_h)|_K = \left| \frac{1}{\text{meas}(K)} \int_K \mathcal{R}_c(\mathbf{u}_h) d\Omega \right|. \quad (35)$$

Now, using the divergence theorem, we can expand the integral of the momentum residual as follows

$$\begin{aligned} \int_K \mathcal{R}_m(\mathbf{u}_h) d\Omega &= \int_K (\mathbf{f} - \partial_t \mathbf{u}_h + \nabla \cdot [-\nu \nabla \mathbf{u}_h + \mathbf{u}_h \otimes \mathbf{u}_h + p \mathbf{I}]) d\Omega \\ &= \int_K (\mathbf{f} - \partial_t \mathbf{u}_h) d\Omega + \int_{\partial K} [-\nu \nabla \mathbf{u}_h + \mathbf{u}_h \otimes \mathbf{u}_h + p \mathbf{I}] \cdot \mathbf{n} d\Gamma. \end{aligned} \quad (36)$$

Likewise, the cell integral of the continuity residual can be expressed as

$$\int_K \mathcal{R}_c(\mathbf{u}_h) d\Omega = - \int_{\partial K} \mathbf{u}_h \cdot \mathbf{n} d\Gamma. \quad (37)$$

Hence, the final expression of the VMS error estimators in a FV framework will be given by

$$\eta_{K,\mathbf{u}} = \text{meas}(K)^{1/2} \tau_{m,L^2}^+ \left| \frac{1}{\text{meas}(K)} \left(\int_K (\mathbf{f} - \partial_t \mathbf{u}_h) d\Omega + \int_{\partial K} [-\nu \nabla \mathbf{u}_h + \mathbf{u}_h \otimes \mathbf{u}_h + p \mathbf{I}] \cdot \mathbf{n} d\Gamma \right) \right|, \quad (38)$$

$$\eta_{K,p} = \text{meas}(K)^{1/2} \tau_{c,L^2}^+ \left| \frac{1}{\text{meas}(K)} \left(- \int_{\partial K} \mathbf{u}_h \cdot \mathbf{n} d\Gamma \right) \right|. \quad (39)$$

In this work, the numerical results obtained using a FV method will be computed in a staggered Cartesian grid. In this case, the pressure unknowns are located at the centre of the cell and the velocity components at the centre of the faces normal to each component (see Figure IV, where a 2D sketch of the FV discretization is depicted, with the notation $\mathbf{u}_h = [u, v]^T$). Since the FV method is a collocation method, the evaluation of

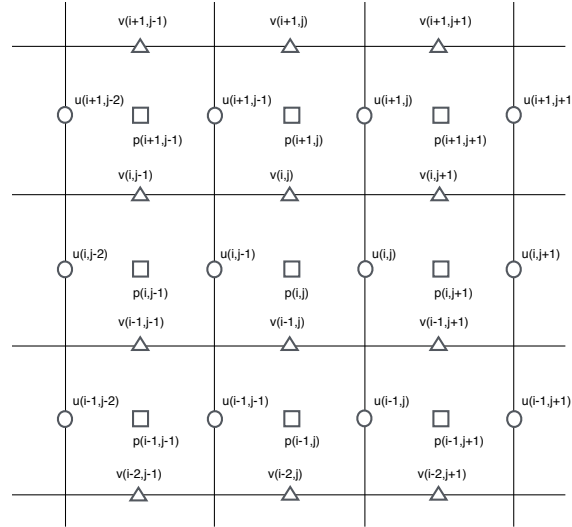


Figure 1. A staggered grid stencil.

the residuals at the collocated points will give a null residual by definition. Therefore, we need to compute the residuals at different collocation points. The velocity error estimator is evaluated at the cell centre for both components, while the pressure error estimator is evaluated at the cell corners.

With this setting, the first integral appearing in equation (38) is evaluated multiplying the cell volume by the quantities evaluated at the cell centres. For this first integral term, the external force term is already defined at the cell centres, while the time derivative of the velocity is evaluated by averaging the velocity values at the faces. For the second term (39), the velocity values and gradients are evaluated at the cell faces, and the pressure is obtained taking an average over the cells adjacent to a face. This second integral term represents a centered evaluation of the residual, because of the structure of the boundary integral (Gauss theorem).

Remark. It can be shown, see [25, Appendix B], that under the following conditions, a FV discretization can be interpreted as a FE discretization:

- The FE space is defined through Raviart-Thomas elements of order 0, i.e. quadrilateral/hexahedra elements with constant pressure and the velocity unknowns defined on the normal component of each face.

- The viscous fluxes are computed using the velocity gradient as an auxiliary variable.
- Time integration is performed with a specific combination of trapezoidal and midpoint rules.

V. Numerical results

In this section we aim to demonstrate the applicability of the VMS error estimators in a FV framework and assess its performance for different flow types. The accuracy and robustness of the VMS error estimators for the compressible NS equations have been successfully conducted in Hauke *et al.*¹²

Although the main goal of this work is the assessment of such error estimators in a FV framework, a first analysis for the steady incompressible NS equations in a FE context will be carried out. Afterwards, a thermally-coupled incompressible flow is tested with a Rayleigh-Bénard convection between a hot and cold walls. Finally, the error estimators are tested for a simplified version of a Scramjet combustor with a compressible NS formulation.

Although the VMS error estimator has been defined for all the fields appearing in the NS equations, here we will focus on the error of the velocity field, $\eta_{K,\mathbf{u}}$.

V.A. Incompressible flow

In order to test the accuracy and robustness of the proposed error estimators, we solve the steady incompressible Navier-Stokes equations in a Finite Element framework, using FEMPAR.²⁶ A first study is performed for a test with a manufactured analytical solution, in which we impose a forcing term such that the solution satisfies the following analytical expression

$$\mathbf{u}_x(x, y) = x^3 y^2, \quad (40)$$

$$\mathbf{u}_y(x, y) = -x^2 y^3, \quad (41)$$

$$p(x, y) = x^2 + y^2. \quad (42)$$

The problem is solved using linear quadrilateral elements in a domain $\Omega = [0, 1] \times [0, 1]$. The FE formulation for the incompressible Navier-Stokes equations is unstable when linear interpolation is used for both velocity and pressure. To overcome these instabilities, a VMS formulation is used for the purpose of numerical stability, see the work done by Hughes.¹⁰

A refinement analysis is performed to assess the convergence rate of the error estimator for three different Reynolds numbers $Re = \{1.0e2, 1.0e3, 1.0e4\}$. The error of the FE method should decay with a 2nd order rate when refining the mesh ($\mathcal{O}(h^{-2})$). In Figure 2 we see that the global estimated error converges following this rate for the three cases.

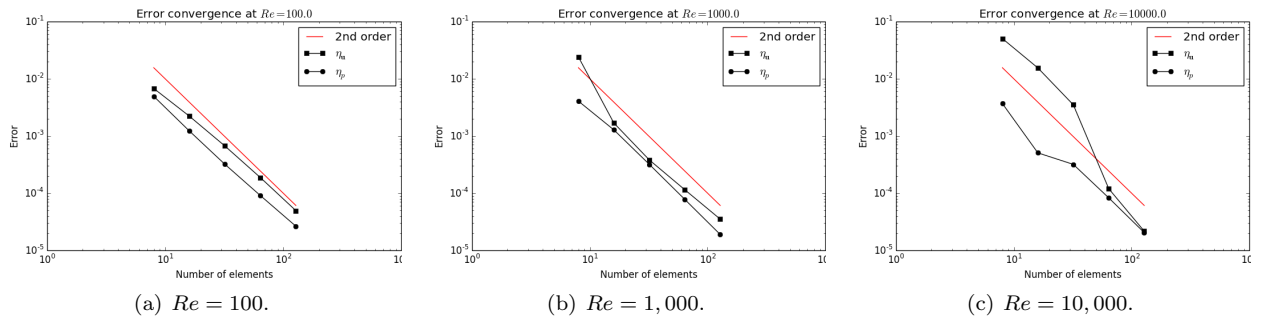


Figure 2. Error estimator convergence in a manufactured analytical solution for different Reynolds number.

The VMS error estimators are local, allowing us to identify the regions in which the error is higher, and based on that, an adaptive refinement strategy could be used to efficiently reduce the global error. In Figure 3 we depict the exact and estimated velocity error values for the case of $Re = 1.0e4$ in a 32^2 quadrilateral elements mesh. The VMS estimator captures the regions in which the exact error is greater, although the error is overestimated. Note that the same color scale has been used for the exact and estimated errors (Figure 3(b) and Figure 3(c)).

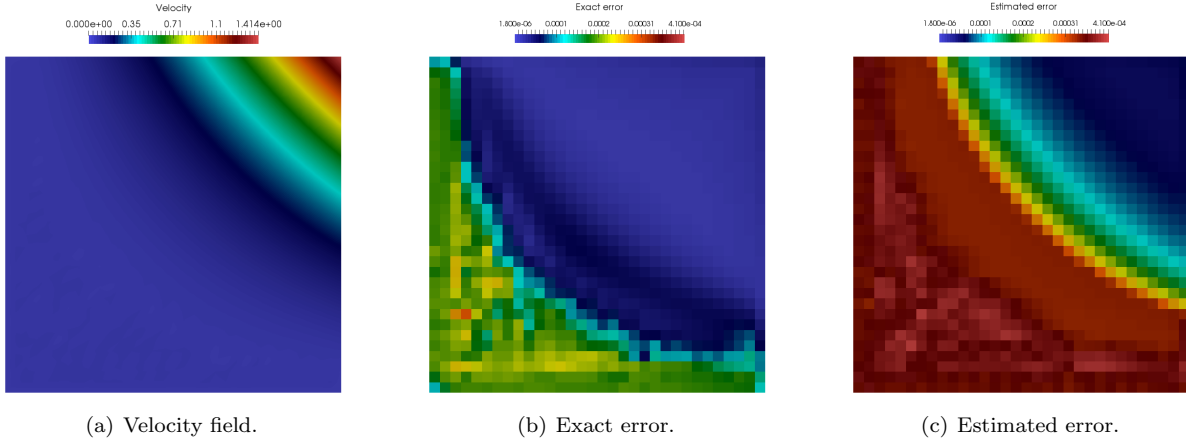


Figure 3. Velocity field, and exact and estimated velocity error in a 32^2 elements mesh for a Reynolds number $Re = 10,000$.

A widely used benchmark test for the validation of numerical approximations of the incompressible NS equations is the driven cavity flow, solved in a domain $\Omega = [0, 1] \times [0, 1]$, imposing an horizontal velocity $\mathbf{u}_x = 1.0$ at the top side and homogeneous Dirichlet boundary conditions on the remaining edges. The problem is solved with a Reynolds number $Re = 100$. A mesh of 32^2 quadrilateral elements has been used for this test. The results of the velocity field and the estimated velocity error are depicted in Figure 4. In this case, we do not have an analytical solution of the velocity field and, therefore, we cannot compare against the exact error. However we see that the estimated error is accumulated at the top corners, where higher velocity and pressure gradients are expected.

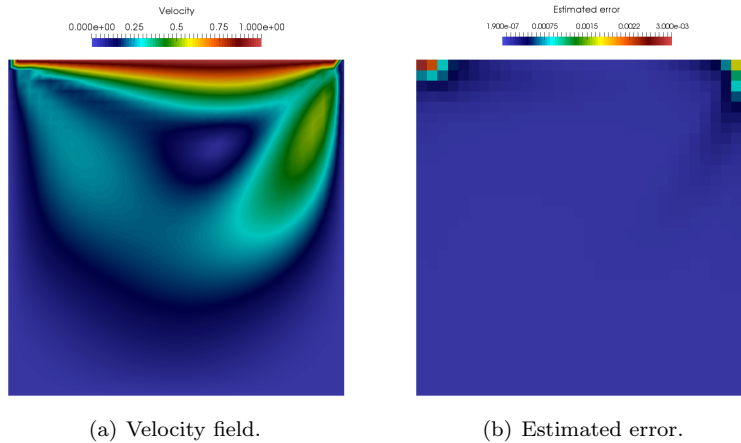


Figure 4. Velocity field and estimated velocity error in a 32^2 elements mesh for the cavity flow with a Reynolds number $Re = 100$.

V.B. Thermally coupled incompressible flow

One of the goals of this work is to demonstrate that the VMS error estimators can be applied in a variety of flow types and that can be implemented in a Finite Volume context. As it has been developed in Section IV, to obtain the VMS error estimator $\eta_{K,\mathbf{u}}$ at any cell K in a FV context, we need to evaluate the cell volume ($\text{meas}(K)$), the time-scale parameter (τ_{m,L^2}^+) and the integral over the cell of the momentum equation residual.

The expression of $\eta_{K,\mathbf{u}}$ for the thermally coupled Navier-Stokes equations is basically the same as (38), but with the difference on the definition of the residual, which in that case reads

$$\mathcal{R}_m(\mathbf{u}_h, p_h, \theta_h) = \mathbf{f} + \alpha \mathbf{g} \theta_0 - [\partial_t \mathbf{u}_h - \nu \Delta \mathbf{u}_h + \mathbf{u}_h \cdot \nabla \mathbf{u}_h + \nabla p_h + \alpha \mathbf{g} \theta_h], \quad (43)$$

where θ_h is the temperature field, α the thermal expansion coefficient, \mathbf{g} the gravity acceleration vector and θ_0 the reference temperature. In a staggered FV grid, the temperature field is collocated at the cell centers, like the pressure field (see Figure IV).

Introducing the residual expression (43) into (30), and following the reasoning developed in Section IV, we obtain an equivalent expression for the velocity VMS error estimator that reads

$$\eta_{K,\mathbf{u}} = \text{meas}(K)^{1/2} \tau_{m,L^2}^+ \left| \frac{1}{\text{meas}(K)} \left(\int_K (\mathbf{f} + \alpha \mathbf{g}(\theta_0 - \theta_h) - \partial_t \mathbf{u}_h) d\Omega + \int_{\partial K} [-\nu \nabla \mathbf{u}_h + \mathbf{u}_h \otimes \mathbf{u}_h + p \mathbf{I}] \cdot \mathbf{n} d\Gamma \right) \right|. \quad (44)$$

In order to showcase the performance of the VMS error estimator for a thermally coupled flow, we solve the well known Rayleigh-Bénard flow between a hot and a cold walls, in a periodic domain as sketched in Figure 5. The physical parameters and the domain setting for this test are summarized in Table 1.

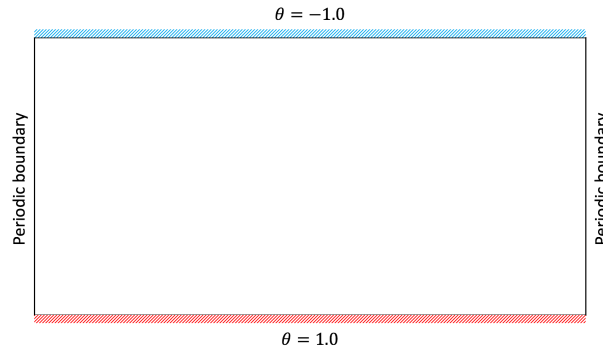


Figure 5. Rayleigh-Bénard test configuration.

In the Rayleigh-Bénard flow simulation, because of the buoyancy phenomena, the initial condition is unstable. This physical instability leads to the formation of convection cells, that after enough time take the form of regular recirculation patterns. In the following figures we plot the state of the flow at different times: at $t = 5$, at the onset of buoyant instabilities near the boundaries, $t = 15$, when the flow is fully developed, and $t = 40$, when buoyant recirculating cells are formed. The results shown here are computed using a Cartesian mesh of 160×80 cells.

Since the VMS error estimator uses as an input the computed velocity, temperature and pressure fields, we will first show the state of this quantities at the prescribed times. In Figure 6, we plot the temperature and pressure fields. Note that the temperature bounds in Figure 6(a), Figure 6(b) and Figure 6(c) are lower than the actual boundary values, $\theta_h = 1.0$ and $\theta_h = -1.0$ at the bottom and top walls, respectively. This is caused by the fact that the temperature and pressure fields are evaluated at the cell centers, and we plot the values in such locations. In Figure 6 we can clearly distinguish the different stages of the flow, where initially, only the flow near the boundary is starting to develop (Figure 6(a) and Figure 6(d)). At $t = 15$ the variations in pressure and temperature have not yet developed the patterns of recirculating cells (Figure 6(b) and Figure 6(e)). Finally, at $t = 40$ (Figure 6(c) and Figure 6(f)) the flow evolves to a regular recirculation pattern.

In Figure 7 we plot the x - and y -components of the velocity. Note that each velocity component is collocated and stored in correspondence of a normal cell face. In particular, since this test is solved on a Cartesian grid, we store the velocity in the x -direction along the vertical faces and the velocity in the y -direction along the horizontal faces. The same behaviour is observed in this figure, where at the initial times (Figure 7(a) and Figure 7(d)) the higher velocity values are concentrated near the boundary. At $t = 15$,

Table 1. Parameter setting for the Rayleigh-Bénard flow test

Parameter	Value
Domain size in x -direction	2.0
Domain size in y -direction	1.0
Rayleigh number	$5.0 \cdot 10^5$
Prandtl number	0.7
Temperature of the bottom wall	1.0
Temperature of the top wall	-1.0
Time step size	$1.0 \cdot 10^{-2}$

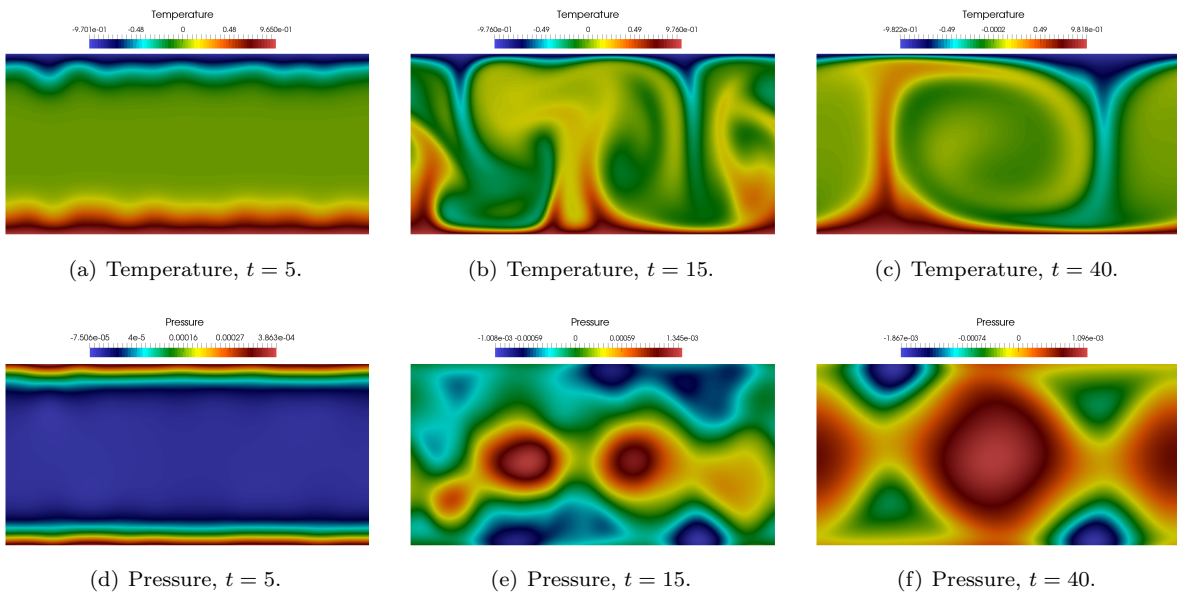


Figure 6. Temperature and pressure fields at the cell centers at different times.

global flow features can be seen in Figure 7(b) and Figure 7(e). Finally, looking at Figure 7(c) and Figure 7(f), a regular recirculation pattern is observed.

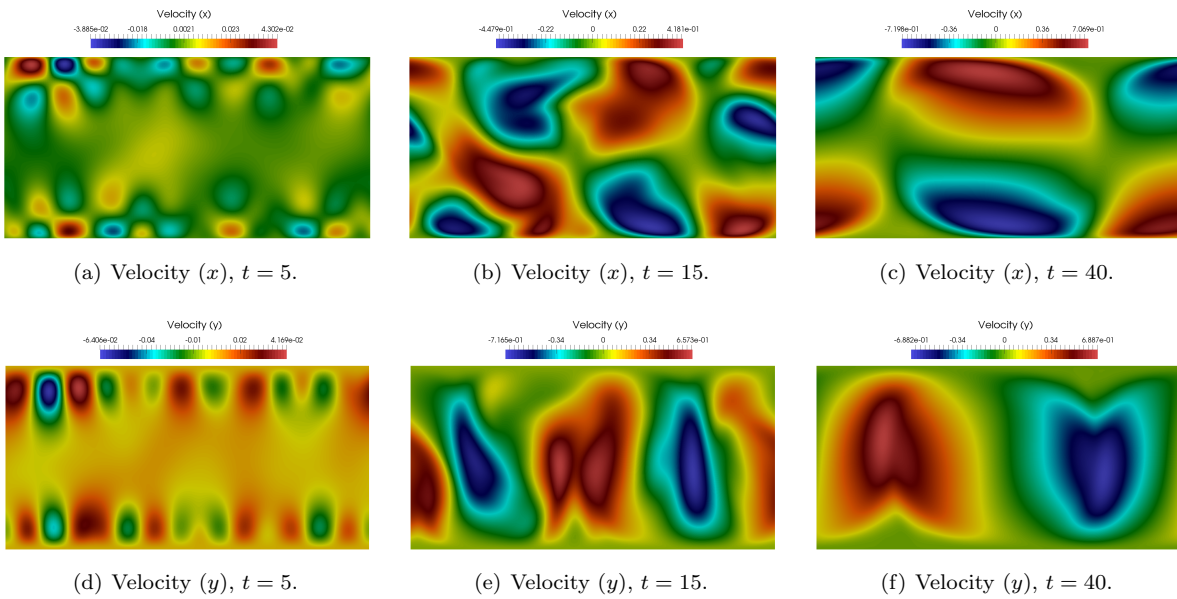


Figure 7. Velocity field components at the cell faces at different times.

Once we have the velocity, temperature and pressure fields, we can evaluate the velocity error estimator, the magnitude of which is depicted in Figure 8. As expected, initially the estimated numerical error is concentrated at the boundaries, where the flow starts developing. When the flow is fully developed, we see that the estimated error is distributed over the whole domain. As more steady recirculating patterns develop, the error is concentrated near upwelling and downwelling jets. Note that at the center of the convection cell (Figure 8(c)) the error is very low, because the flow is nearly quiescent in that region.

In Figure 9 we depict the evolution of the global error estimator, integrated over all the domain, for three different grids constructed through two consecutive uniform refinements. As we can see, the error is increased as the flow starts to develop, achieving a stationary value when the convection cells are generated. We can also observe that the error magnitude decays at least quadratically as the grid is refined.

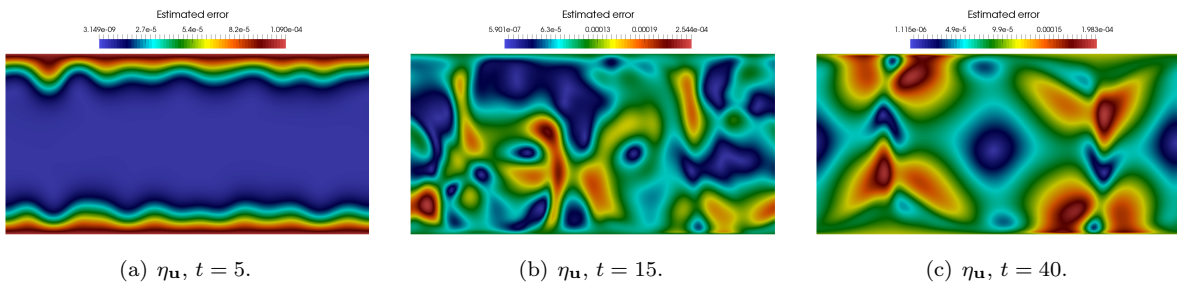


Figure 8. Estimated error field at the cell centers at different times.

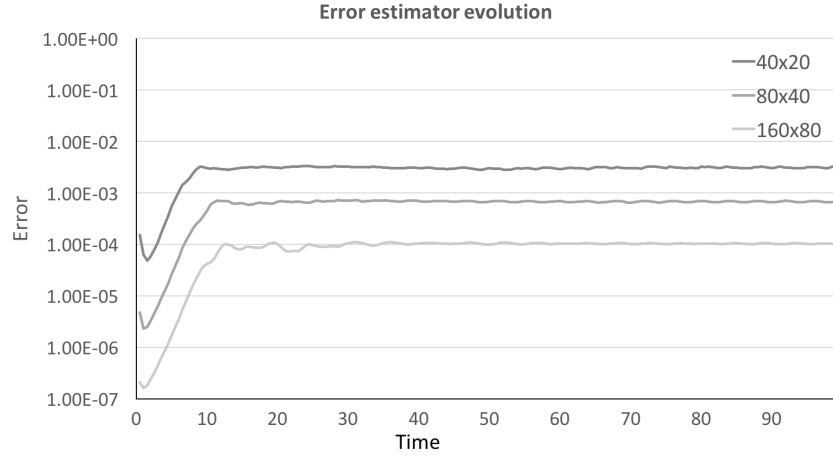


Figure 9. Error estimator η_u evolution over time for different discretizations.

V.C. Scramjet combustor simulation

As a last test, we apply the VMS error estimators to a more realistic and complex problem such as the simulation of a Scramjet combustor, related to the Hypersonic International Flight Research Experiment (HIFiRE).^{27,28} In particular, a simplified version of the HIFiRE Direct Connect Rig (HDCR)²⁹ (Figure V.C) is considered in this section.

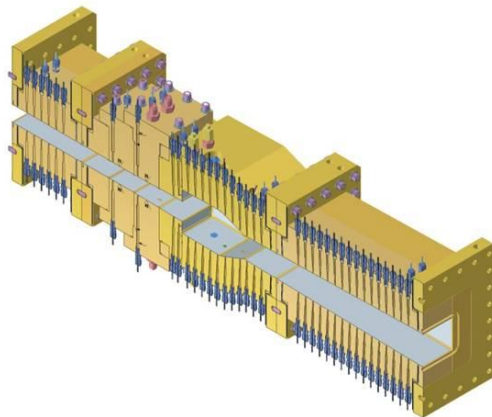
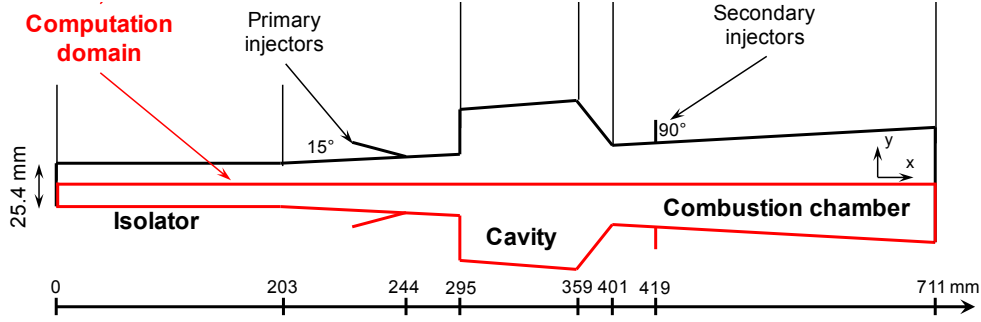


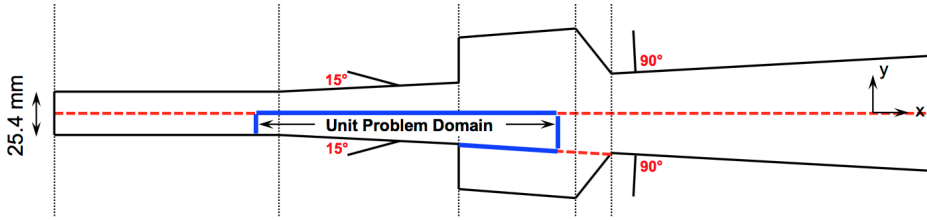
Figure 10. HDCR geometry given in Cabell et al.²⁹

We solve the problem in two dimensions, with a geometry as indicated by the blue lines in Figure 11(b). The flow travels from left to right (along the x direction), and there are two different fuel injectors, the

primary on the left side of the cavity with an angle of 15° , and a secondary injector after the cavity. A simple geometry without cavity will be considered (as shown in Figure 11(b)), where only the primary injector is contemplated. In that case the chemistry is initially disabled, allowing a targeted investigation of the interaction between the fuel jet and the supersonic crossflow without the effects of combustion reaction.



(a) HDCR two-dimensional geometry.



(b) Simplified two-dimensional geometry

Figure 11. Two-dimensional geometry used in the simulations.

The resolution of this problem is carried out using RAPTOR, a FV software developed by Oefelein,³⁰ solving the fully-coupled conservation equations of mass, momentum, total-energy, and species for a chemically reacting flow. A Large Eddy Simulation (LES) model is considered to model the turbulent phenomena, see Oefelein *et al.*³¹ Some of the flow properties used in this simulation are specified in Table 2, and more details on the inflow conditions can be found in the work done by Lacaze *et al.*³²

Table 2. Parameter setting for the Scramjet combustor test

Parameter	Value
Dynamic Viscosity	$36.4 \cdot 10^{-6} \text{ Pa} \cdot \text{s}$
Bulk Velocity	1340 m/s
Speed of Sound	533m/s
Reynolds Number	189,000
Prandtl Number	0.693

The definition of the VMS error estimator in this case, for the velocity field, is based on the residual of the full NS momentum equation for compressible flows, which reads

$$\mathcal{R}_m(\mathbf{u}_h, p_h, \rho_h) = \mathbf{f} - \left[\partial_t(\rho_h \mathbf{u}_h) - \mu \nabla \cdot \left[(\nabla \mathbf{u}_h + \nabla \mathbf{u}_h^T) - \frac{2}{3} \nabla \cdot \mathbf{u}_h \mathbf{I} \right] + \rho_h \mathbf{u}_h \cdot \nabla \mathbf{u}_h + \nabla p_h \right], \quad (45)$$

with ρ_h the density field. With this definition, the equivalent expression for the velocity VMS error estimator will be given by

$$\eta_{K,\mathbf{u}} = \text{meas}(K)^{1/2} \tau_{m,L^2}^+ \left| \frac{1}{\text{meas}(K)} \left(\int_K (\mathbf{f} - \partial_t(\rho_h \mathbf{u}_h)) d\Omega + \int_{\partial K} \left[-\mu \left[(\nabla \mathbf{u}_h + \nabla \mathbf{u}_h^T) - \frac{2}{3} \nabla \cdot \mathbf{u}_h \mathbf{I} \right] + \rho_h (\mathbf{u}_h \otimes \mathbf{u}_h) + p_h \mathbf{I} \right] \cdot \mathbf{n} d\Gamma \right) \right|. \quad (46)$$

In this case, the velocity VMS error estimator relies on the velocity, pressure and density values obtained from the resolution of the problem in a FV code. This fields are shown in Figure 12 for the simplest geometry, computed in a structured grid with 403×32 cells. In this figure we clearly see the shock train generated at the primary injector position. It can also be observed that the velocity field presents some fluctuations between

the inlet and the primary injector, coming from the fluctuating velocity imposed at the inlet. Another feature that we can highlight looking at Figure 12 is the wake that is formed after the primary injector, and can be more clearly noticed in the horizontal velocity field.

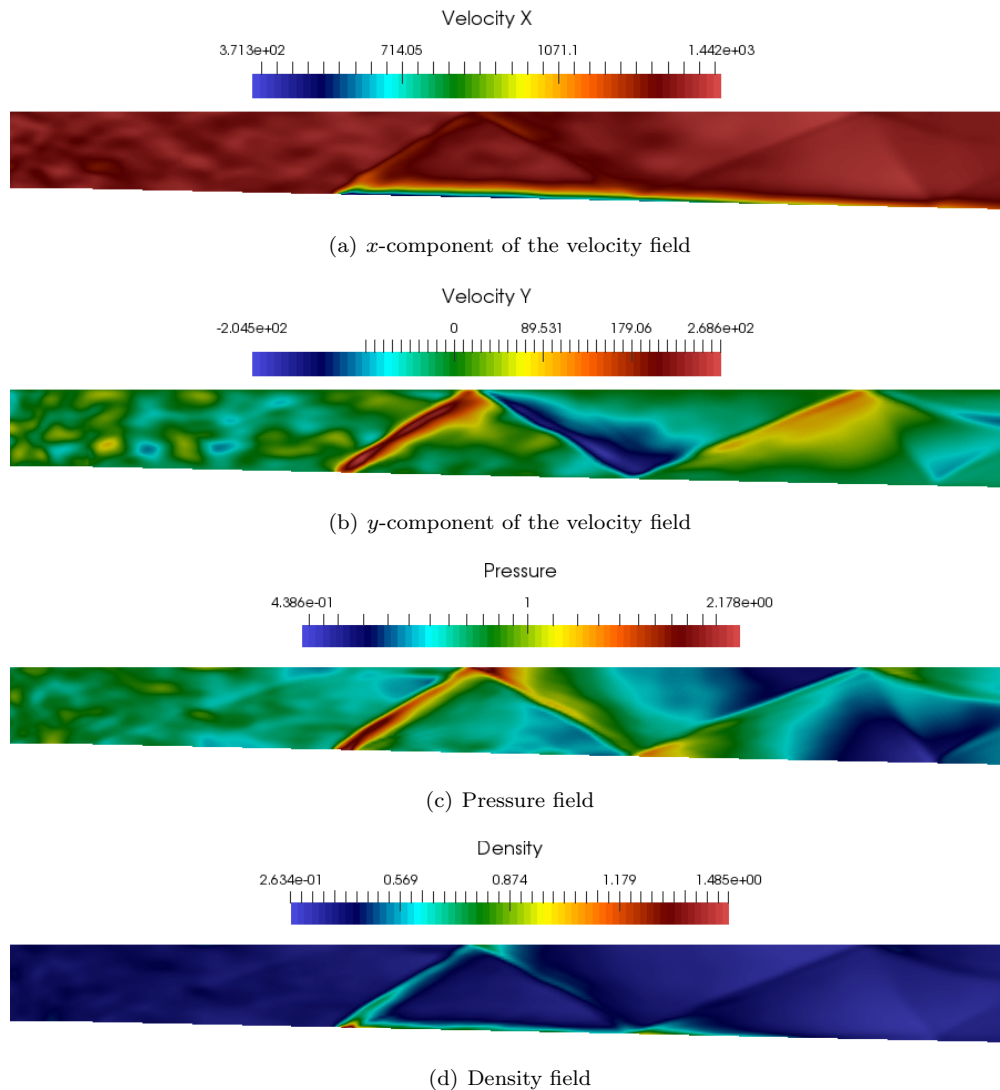


Figure 12. Fields obtained from the FV simulation at a given time

In Figure 13 we depict the value of the VMS error estimators for the velocity field (in the horizontal and vertical directions) at the same time step as the one at which we have plotted the results shown in Figure 12, both for the simplest geometry case. We can see that the larger error values occur for the x -component, which is also the component with higher velocity values. Note that the error estimator captures the velocity fluctuations appearing between the inlet and the first injector, and the shock train after the first injector. We can also notice higher error values in the wake of the primary injector, where a turbulent boundary layer is generated.

VI. Conclusions and future work

In this work we have described the extension of the VMS error estimators to a FV framework and applied to the NS equations, for incompressible, thermally-coupled and compressible conditions.

As an starting point, in Section II, we have described the VMS method in a FE framework for the incompressible NS equations, allowing us to set the notation that have been used a posteriori. In Section III we have described the steps followed to obtain an error estimator for the NS equations, which have been

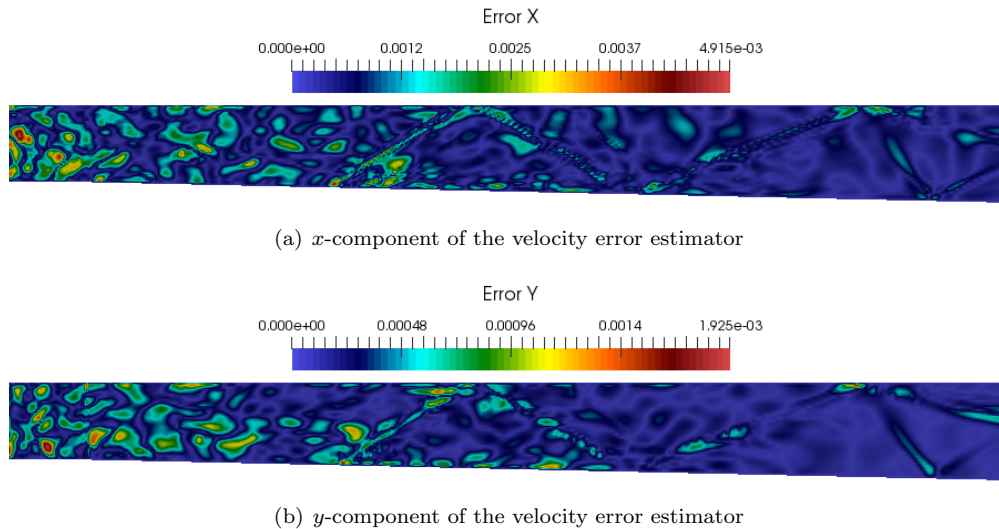


Figure 13. Velocity error estimators in the x (top) and y (bottom) components.

already described in the literature.

Previous contributions can be found in the literature regarding the definition and assessment of the VMS error estimators for the Navier-Stokes equations in a FE context, but its application to a FV method was still unexplored. The description of such error estimators in a FV context has been stated in Section IV. To build the error estimators in a FV framework we have assumed constant residuals over the grid cells and neglected the inter-element contributions to the error estimator.

A first test has been done using a FE method in which we show that the error estimator gives the appropriate rates of convergence. We have later applied to a thermally-coupled Rayleigh-Bénard flow between a hot and cold walls. We have shown that the error estimator is able to capture the locations in which the flow develops larger variability. We have also shown that the error estimator converges as the grid is refined.

Finally, we have applied the VMS error estimators to a more complex problem, where a simplified version of a Scramjet combustor is simulated. In this case, we have seen that the error estimator gives higher values at the initial part of the duct, where higher velocity fluctuations appear, and in the shock train.

Further investigations have to be conducted to assess of the robustness of the VMS error estimators for the NS equations in a FV framework. Note that the robustness of this error estimators in a FE framework has been assessed for the compressible NS equations, but its robustness for the incompressible case still remains unclear.

Furthermore, the application of the VMS error estimators to a full Scramjet problem is still to be done. Nevertheless, the definition of the VMS error estimators extends naturally to a three-dimensional geometry.

Aknowledgements

Support for this research was provided by the Defense Advanced Research Projects Agency (DARPA) program on Enabling Quantification of Uncertainty in Physical Systems (EQUIPS) led by Dr. Fariba Fahroo, Program Manager. The second author would like also to thank Dr. Pietro Congedo at INRIA-Bordeaux/Sud-Ouest for valuable discussions and suggestions.

References

- ¹Celik, I., Klein, M., Freitag, M., and Janicka, J., “Assessment measures for URANS/DES/LES: an overview with applications,” *Journal of Turbulence*, Vol. 7, 2006, pp. N48.
- ²Rebba, R., Mahadevan, S., and Huang, S., “Validation and error estimation of computational models,” *Reliability Engineering & System Safety*, Vol. 91, No. 10, 2006, pp. 1390–1397.
- ³Roache, P. J., “Quantification of Uncertainty in Computational Fluid Dynamics,” *Annual Review of Fluid Mechanics*, Vol. 29, No. 1, 1997, pp. 123–160.
- ⁴Oden, J. T., Babuška, I., Nobile, F., Feng, Y., and Tempone, R., “Theory and methodology for estimation and control of

errors due to modeling, approximation, and uncertainty,” *Computer Methods in Applied Mechanics and Engineering*, Vol. 194, No. 2, 2005, pp. 195–204.

⁵Babuška, I. and Rheinboldt, W. C., “A-posteriori error estimates for the finite element method,” *International Journal for Numerical Methods in Engineering*, Vol. 12, No. 10, 1978, pp. 1597–1615.

⁶Ainsworth, M. and Oden, J. T., *A Posteriori Error Estimation in Finite Element Analysis*, John Wiley & Sons, 2011.

⁷Roy, C., “Review of Discretization Error Estimators in Scientific Computing,” *48th AIAA Aerospace Sciences Meeting Including the New Horizons Forum and Aerospace Exposition*, American Institute of Aeronautics and Astronautics.

⁸Verfürth, R., “A posteriori error estimates for nonlinear problems. Finite element discretizations of elliptic equations,” *Mathematics of Computation*, Vol. 62, No. 206, 1994, pp. 445–475.

⁹Hauke, G., Doweidar, M. H., and Miana, M., “The multiscale approach to error estimation and adaptivity,” *Computer Methods in Applied Mechanics and Engineering*, Vol. 195, No. 13, 2006, pp. 1573–1593.

¹⁰Hughes, T. J. R., “Multiscale phenomena: Green’s functions, the Dirichlet-to-Neumann formulation, subgrid scale models, bubbles and the origins of stabilized methods,” *Computer Methods in Applied Mechanics and Engineering*, Vol. 127, No. 1, 1995, pp. 387–401.

¹¹Hauke, G., Fuster, D., and Doweidar, M. H., “Variational multiscale a-posteriori error estimation for multi-dimensional transport problems,” *Computer Methods in Applied Mechanics and Engineering*, Vol. 197, No. 33, 2008, pp. 2701–2718.

¹²Hauke, G., Fuster, D., and Lizarraga, F., “Variational multiscale a posteriori error estimation for systems: The Euler and Navier-Stokes equations,” *Computer Methods in Applied Mechanics and Engineering*, Vol. 283, 2015, pp. 1493–1524.

¹³Irisarri, D. and Hauke, G., “A posteriori pointwise error computation for 2-D transport equations based on the variational multiscale method,” *Computer Methods in Applied Mechanics and Engineering*, Vol. 311, 2016, pp. 648–670.

¹⁴Bazilevs, Y., Calo, V. M., Cottrell, J. A., Hughes, T. J. R., Reali, A., and Scovazzi, G., “Variational multiscale residual-based turbulence modeling for large eddy simulation of incompressible flows,” *Computer Methods in Applied Mechanics and Engineering*, Vol. 197, No. 1, 2007, pp. 173–201.

¹⁵Colomés, O., Badia, S., Codina, R., and Principe, J., “Assessment of variational multiscale models for the large eddy simulation of turbulent incompressible flows,” *Computer Methods in Applied Mechanics and Engineering*, Vol. 285, 2015, pp. 32–63.

¹⁶Rasthofer, U. and Gravemeier, V., “Recent Developments in Variational Multiscale Methods for Large-Eddy Simulation of Turbulent Flow,” *Archives of Computational Methods in Engineering*, 2017, pp. 1–44.

¹⁷Codina, R., Principe, J., and Ávila, M., “Finite element approximation of turbulent thermally coupled incompressible flows with numerical subgrid scale modelling,” *International Journal of Numerical Methods for Heat & Fluid Flow*, Vol. 20, No. 5, 2010, pp. 492–516.

¹⁸Koobus, B. and Farhat, C., “A variational multiscale method for the large eddy simulation of compressible turbulent flows on unstructured meshes application to vortex shedding,” *Computer Methods in Applied Mechanics and Engineering*, Vol. 193, No. 15, 2010, pp. 1367–1383.

¹⁹Hughes, T. J. R., Franca, L. P., and Balestra, M., “A new finite element formulation for computational fluid dynamics: V. Circumventing the babuška-brezzi condition: a stable Petrov-Galerkin formulation of the stokes problem accommodating equal-order interpolations,” *Computer Methods in Applied Mechanics and Engineering*, Vol. 59, No. 1, 1986, pp. 85–99.

²⁰Codina, R., “Stabilized finite element approximation of transient incompressible flows using orthogonal subscales,” *Computer Methods in Applied Mechanics and Engineering*, Vol. 191, No. 39, 2002, pp. 4295–4321.

²¹Codina, R., “On stabilized finite element methods for linear systems of convection-diffusion-reaction equations,” *Computer Methods in Applied Mechanics and Engineering*, Vol. 188, No. 1, 2000, pp. 61–82.

²²Codina, R., “Analysis of a stabilized finite element approximation of the Oseen equations using orthogonal subscales,” *Applied Numerical Mathematics*, Vol. 58, No. 3, 2008, pp. 264–283.

²³Codina, R., Principe, J., and Baiges, J., “Subscales on the element boundaries in the variational two-scale finite element method,” *Computer Methods in Applied Mechanics and Engineering*, Vol. 198, No. 5, 2009, pp. 838–852.

²⁴Hauke, G., Doweidar, M. H., and Miana, M., “Proper intrinsic scales for a-posteriori multiscale error estimation,” *Computer Methods in Applied Mechanics and Engineering*, Vol. 195, No. 33, 2006, pp. 3983–4001.

²⁵Calo, V., *Residual-based multiscale turbulence modeling: finite volume simulations of bypass transition*.

²⁶Badia, S., Martín, A. F., and Principe, J., “FEMPAR: An Object-Oriented Parallel Finite Element Framework,” *Archives of Computational Methods in Engineering*, 2017, pp. 1–77.

²⁷Dolvin, D., “Hypersonic International Flight Research and Experimentation (HIFiRE) Fundamental Science and Technology Development Strategy,” *15th AIAA International Space Planes and Hypersonic Systems and Technologies Conference*, American Institute of Aeronautics and Astronautics.

²⁸Schmisser, J. D., “Hypersonics into the 21st century: A perspective on AFOSR-sponsored research in aerothermodynamics,” *Progress in Aerospace Sciences*, Vol. 72, 2015, pp. 3–16.

²⁹Hass, N., Cabell, K., Storch, A., and Gruber, M., “HIFiRE Direct-Connect Rig (HDCR) Phase I Scramjet Test Results from the NASA Langley Arc-Heated Scramjet Test Facility,” *17th AIAA International Space Planes and Hypersonic Systems and Technologies Conference*, American Institute of Aeronautics and Astronautics, 2011.

³⁰Oefelein, J. C., “Large eddy simulation of turbulent combustion processes in propulsion and power systems,” *Progress in Aerospace Sciences*, Vol. 42, No. 1, 2006, pp. 2–37.

³¹Oefelein, J. C., Schefer, R. W., and Barlow, R. S., “Toward Validation of Large Eddy Simulation for Turbulent Combustion,” *AIAA Journal*, Vol. 44, No. 3, 2006, pp. 418–433.

³²Lacaze, G., Vane, Z., and Oefelein, J. C., “Large Eddy Simulation of the HIFiRE Direct Connect Rig Scramjet Combustor,” *55th AIAA Aerospace Sciences Meeting*, American Institute of Aeronautics and Astronautics.